Catena 208 (2022) 105738

Contents lists available at ScienceDirect

Catena

journal homepage: www.elsevier.com/locate/catena

Provenance fingerprints of atmospheric dust collected at Granada city (Southern Iberian Peninsula). Evidence from quartz grains

A. Molinero-García, J.M. Martín-García *, M.V. Fernández-González, R. Delgado

Departamento de Edafología y Química Agrícola, Universidad de Granada, Campus Cartuja, 18071 Granada, Spain

ARTICLE INFO

Keywords:
Quartz
Shape parameters
Atmospheric dust
Provenance fingerprint
Dust mineralogy
Dust geochemistry

ABSTRACT

Dust in the Earth's atmosphere is increasing, particularly in southern Spain. The study of dust properties allows for a hypothesis on the origin and provenance of dust. This study characterised atmospheric dust deposited in the city of Granada (south of Spain) during three spring periods (samples 4PA, 16PA, and 28PA, collected in 2012, 2013, and 2014, respectively). The aim was to ascertain dust characteristics and genesis using a set of methodological techniques. The backward trajectories study separated the samples into two groups: scarce Saharan influence (sample 16PA, 6% of backward trajectories are from, or have passed through, Africa) and greater influence (samples 4PA and 28PA, 26% and 33%, respectively). This grouping was verified by the rest of the properties analysed, namely, PM10 concentration, deposition rates, grain size, mineralogy, and elemental composition (minor, including rare earth elements). In addition, mineral quartz showed differences in particle morphology and surface microtextures. The mineralogical and geochemical studies of our samples have proved similarities with other dust collected in Granada and soils from the Iberian Peninsula. The principal component analysis of the quartz shape parameters insists on the differentiation of these groups. We propose the morphoscopy of quartz grains (a significant component of atmospheric dust) as a fingerprint of provenance.

1. Introduction

Atmospheric dust is one of the most abundant aerosols globally and an essential component of the Earth's environmental system (Nickovic et al., 2012; Muhs et al., 2014; Schepanski, 2018). The Sahara Desert is the world's largest source of atmospheric dust (50%–70% of total emissions worldwide), contributing between 1 and 3 billion tons per year (Prospero et al., 2002; Engelbrecht et al., 2016; Huneeus et al., 2011; Russo et al., 2020). African dust intrusion should be considered in the Iberian Peninsula because of the proximity of the Sahara Desert (e.g. Valenzuela et al., 2012).

Granada city (south of the Iberian Peninsula) has one of Spain's highest atmospheric pollution levels. The primary pollutants are particulate matter (PM) and NOx (Ministry for Ecological Transition and Demographic Challenge, 2019). PM < 10 μm (PM10) concentration in Granada frequently exceeds both the limit value recommended by the World Health Organization (WHO) (20 μg m^{-3}) and the one-day limit value (50 μg m^{-3}) established by the European Union Directive (2008/50/EC) — the limits were exceeded 54 days per $year^{-1}$ in the period 2010–2020 (Junta de Andalucía, 2021a). Granada's location (a depression surrounded by mountains) favours the development of thermal inversions and weak winds, which boost PM values. PM is a major problem and an environmental risk to health that has concerned the Spanish government since it was classified as a carcinogen to humans (Group 1) (WHO, 2013a; WHO, 2018).

According to the Environmental Protection Agency, PM (also called particle pollution) is a mixture of solid particles and liquid droplets found in the air. PM can be produced by wind erosion of arid and semiarid soil surfaces (Menut et al., 2013) and transported to areas far from their origin. Soils play a critical role in dust production mechanisms (Marticorena, 2014; Wang et al., 2018; Wang et al., 2021). The mineral fraction of aerosols is determined by the mineral composition of the soil they are from (Nickovic et al., 2012; Journet et al., 2014).

Annual atmospheric dust deposition rates are variables in the surrounding areas of Spain, ranging from 137 × 10^3 to 3340 × 10^3 g m^2 (Goudie and Middleton, 2001). These values fluctuate throughout the year. There is a strong interannual variability in the deposition rates (Rodríguez et al., 2015). In some Spanish places, the spring period shows high deposition rates (Gelado-Caballero et al., 2012; Engelbrecht et al., 2014; Cerro et al., 2020); hence, this study has value. Backward

* Corresponding author.
E-mail address: jmmartingarcia@ugr.es (J.M. Martín-García).

https://doi.org/10.1016/j.catena.2021.105738
Received 14 June 2021; Received in revised form 13 September 2021; Accepted 15 September 2021
Available online 1 October 2021

Table 1
General characteristics of dust samples and PM10[1] concentration.

Sample	Period	Deposition rate (mg m^{-2} day^{-1})	PM10 (μg m^{-3})	African backward trajectories (%)
4PA	26/04/2012–31/05/2012	114	23.33	26
16PA	10/05/2013–13/06/2013	159	22.00	6
28PA	16/05/2014–18/06/2014	108	25.33	33

[1] According to Junta de Andalucía (2021b).

trajectories (e.g. Lyamani et al., 2005; Valenzuela et al., 2012), grain size (e.g. Goudie and Middleton, 2001), mineralogy (e.g. Hojati et al., 2012; Scheuvens et al., 2013) and chemical composition (e.g. Xie et al., 2018; Cerro et al., 2020) analyses have been conducted to ascertain the properties and genesis of atmospheric dust, highlighting its provenance. Image analysis (IA) applied to mineral dust SEM images has been widely used (Kalashnikova and Sokolik, 2004; Scheuvens and Kandler, 2014). These techniques are necessary for the characterisation of atmospheric dust.

The specific process of mineral genesis in the atmosphere is notable. Baker et al. (2014) affirmed that atmospheric transport alters the chemical composition of mineral particles, generating layers on mineral dust particle surfaces. Díaz-Hernández and Párraga (2008) and Párraga et al. (2021) have demonstrated the formation of Iberulites in the atmosphere by the coalescence of particles transported by the wind. Likewise, these authors have proved atmospheric mineral neoformation, namely, halite (NaCl) or gypsum ($CaSO_4{\cdot}2H_2O$), due to dissolution and precipitation processes on atmospheric mineral particle surfaces. Costa et al. (2013) and Vos et al. (2014) have reported the formation of an amorphous silica layer on the surfaces of aeolian quartz grains due to high-energy aeolian collisions.

Quartz is a primary constituent of the Earth's crust and surface environment (Strunz and Tennyson, 1982; Drees et al., 1989). It is also a significant component of atmospheric dust (Shentil Kumar and Rajkumar, 2014; Menéndez et al., 2014; Blondet et al., 2019; Candeias et al., 2020). Moreover, morphological characteristics (e.g. microtextures) analysed by Scaning Electron microscopy (SEM) have been widely used in provenance studies of geological materials (Mahaney, 2002; Delgado et al., 2003; Vos et al., 2014; Kemnitz and Lucke, 2019). However, few studies have analysed atmospheric quartz using SEM-IA (e.g. Kandler et al., 2007).

This study analyses the atmospheric dust collected during three consecutive spring periods (2012, 2013, and 2014) in Granada (south of the Iberian Peninsula), a southern European area of interest. Atmospheric dust characterisation is investigated using a wide variety of complementary techniques, namely, backward trajectory studies, laser granulometry (grain size), X-ray diffraction (XRD) mineralogy, and inductively coupled mass spectrometry (ICP-MS), for minor element composition. This set of techniques is novel in research on possible provenance fingerprints. Our study is the first, according to our review of the literature, to attempt a morphological study (shape parameters by SEM-EDX-IA) and surface microtextures study (SEM) of atmospheric quartz grains. The shape parameters of quartz particles were used as indicators of atmospheric dust provenance.

2. Sampling and methods

2.1. Sampling site

The sampling site was the Cartuja University campus (Granada) near the Andalusian Institute of Geophysics (IAG) (37° 11′ 23.5″ N, 3° 35′ 43.7″ W) at 775 m.a.s.l.

Granada is encased in a natural basin surrounded by limestone-dolomitic and siliceous mountains (Vera, 2004) in the southeast of the Iberian Peninsula (~50 km from the Mediterranean coast). It is affected by air masses from both the African continent and Atlantic Ocean. It has an average annual temperature of 15.4 °C and a total average annual precipitation of 365 mm (AEMET, 2020). According to the Köppen climate classification, the climate is a transition between the temperate Mediterranean and dry semiarid.

2.2. Air particulate Matter < 10 μm (PM10) concentration

Particulate matter < 10 μm (PM10) concentration data were obtained through the *Red de Vigilancia de la Calidad del Aire de Andalucía* (Table 1) (Junta de Andalucía, 2021b). The measurement stations used (close to the sampling area) were Palacio de Congresos, Granada Norte, and Ciudad Deportiva. PM10 samples were collected on quartz filters by a Digitel Aerosol Sampler (model DPA14) operated at an average flow rate of 2.3 m^3 h^{-1} (55.2 m^3 day^{-1}).

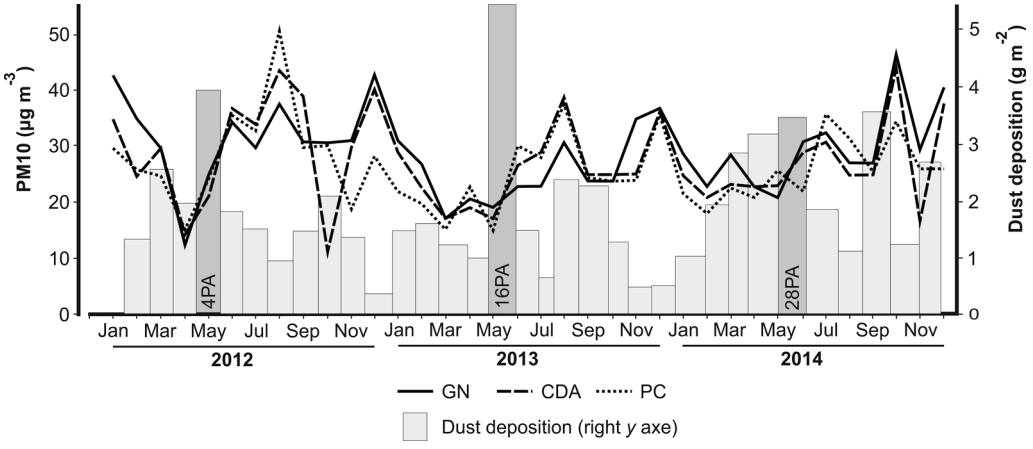

Fig. 1. PM10 monthly concentration (μg/m^3) (data from *Red de Vigilancia de la Calidad del Aire*; Junta de Andalucía, 2021b) and dust deposition (g/m^2) between 2012 and 2014. Boxes show the study sample periods. CDA, Ciudad Deportiva Armilla station; GN, Granada Norte station; PC, Palacio Congresos station.

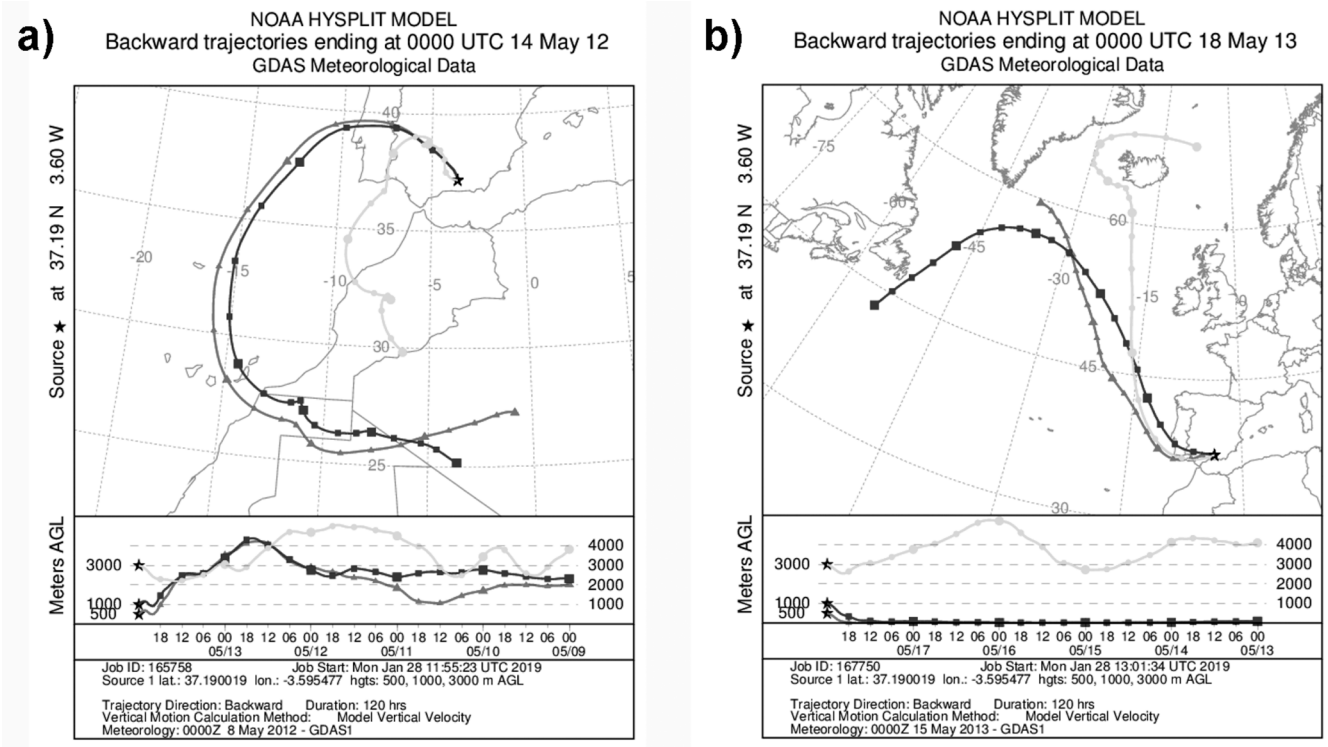

Fig. 2. Examples of backward trajectories in the sampling periods: a) 14 May 2012 (4PA sample) from north of Africa, and b) 18 May 2013 (16 PA sample) from the Atlantic Ocean.

2.3. Hybrid single-particle lagrangian integrated trajectory (HYSPLIT) backwards trajectories

The origin of the air masses reaching Granada city was determined by the transport and dispersion HYSPLIT model. The model is an open, online resource provided by the National Oceanic and Atmospheric Administration Air Resources Laboratory (http://www.arl.noaa.gov/ready.html) (Draxler, 2011). It is the most extensively used model for determining atmospheric transport and dispersion (Reche et al., 2018). HYSPLIT backward trajectories were obtained using archived data from the Global Data Assimilation System with a 120-h run time at 500, 1500, and 3000 m.a.s.l. Daily backward trajectories were determined for each sampling period. The number of days (expressed as a percentage) in which air mass intrusions are from (or have passed through) Africa was calculated.

2.4. Atmospheric dust sampling

The samples (dry and wet deposition) were collected in three periods of 30–35 days by a standard sedimentable particles sampler (model MCV PS) consisting of a metallic structure (tripod form) that connects a collecting funnel (upper part) with a tank (lower part) where the sample was collected. Deposition rates were calculated after drying the samples at 35 °C by weighing each sample (g) and considering the surface (m^2) of the standard dust collector. The study focused exclusively on three late spring periods (from 2012 to 2014; Table 1) because they showed the maximum dust deposition rates (Fig. 1) and a sufficient quantity of dust to perform the set of techniques.

2.5. Atmospheric dust samples study

2.5.1. Particle size distribution

We determined (range 0.02–2000 μm) by wet dispersion laser diffraction method (Mastersizer 2000, Malvern Instruments Ltd., UK). The results were grouped (in μm) as follows: <1, 1–2.5, 2.5–10, <10 (PM10), 10–100, 100–1000 and 1000–2000. Statistical analysis was performed using the free software GRADISTAT (v. 9.1) (http://www.kpal.co.uk/gradistat.html) (Blott and Pye, 2001).

2.5.2. Mineralogical composition

Qualitative and semi-quantitative analysis by X-ray diffraction (XRD) with a Brucker AXS D8 Advance equipment (Cu-Kα radiation, between 3 and 70° 2θ; speed 2° min-1) was performed. The diffractograms were interpreted using the Xpowder software (Martin-Ramos, 2004). The presence of palygorskite was tested at the 0.63 nm peak (d_{200}; 15% intensity). Percentages of minerals were estimated using intensity factors from Schultz (1964), Barahona (1974), and Delgado et al. (1982).

Mineralogical compositions are represented in the triangle Carbonates (calcite + dolomite) —Tectosilicates (quartz + K-feldspar + plagioclase) — Phyllosilicates + Fe oxides (hematite + goethite) (Calero et al., 2009).

2.5.3. Quartz grains study

A morphological study (including microtextures) was performed in approximately 50 quartz grains per sample (a total of 156 quartz grains). Samples were sprinkled on double-sided carbon adhesive tape attached to an aluminium sample stubholder. Next, they were metallised with carbon using a Polaron CC7650 metalliser, and images were obtained by SEM (Hitachi S-510). EDX microanalysis (Rontec) coupled with SEM was used to guarantee the quartz nature of the grains.

First, SEM images were used to detect the quartz surface microtextures. A template (spreadsheet) was created to assess the presence or absence of microtextures (heuristic appreciation), following Mahaney (2002), Vos et al. (2014), and Sweet and Brannan (2016).

Second, SEM images were subjected to IA using ImageJ Software free software (https://imagej.net/) (Abramoff et al., 2004). Particles were separated from the background using image-processing techniques (Kumara et al., 2012). The following shape parameters were calculated: area, perimeter, maximum feret (maxferet), minimum feret (minferet),

Table 2
Deposition rate of dust samples.

	Location	Reference	Period	Deposition rates (mg m^{-2} day^{-1})	
				range	mean
This study	Granada	4PA	26-April to 31-May 2012		114
	Granada	16PA	10-May to 13-June 2013		159
	Granada	28PA	16-May to 18-June 2014		108
Spain (Iberian Peninsula)	Granada	Díaz-Hernández and Miranda-Hernández (1997)	whole year 1992	10–158	63
	Granada	Díaz-Hernández and Párraga (2008)	summer 2001,2002 and 2004	1–82	53
	Granada	Díaz-Hernández and Párraga (2008)	1- to 2-April 2005	113	
	Granada	Díaz-Hernández et al. (2011)	whole year 1992	12–160	71
	Granada (Sierra Nevada)	Morales-Baquero et al. (2013)	December 2000-December 2002	1–132	30
	Granada	Párraga et al. (2021)	June to October 2010	23–168	55
	Barcelona	Lequy et al. (2018)	May 2011 to December 2012	20–320	50
	Barcelona	Avila et al. (1997)	1983–1994		15
Spain (Canary Islands)	Gran Canaria	Menéndez et al. (2007)	October 2002 – October 2003	24–432	108
	Gran Canaria	Menendez et al. (2009)	2003 – 2007	38–120	
Europe (continent)	France (French Forest)	Lequy et al. (2013)	December 2009 – March 2012		5
	France (Alps)	Goudie and Middleton (2001)	30 years ice core		1
	Switzerland (Alps)	Goudie and Middleton (2001)	50 years ice core		1
Europe (Mediterranean islands and seas)	France (Corsica)	Díaz-Hernández and Miranda-Hernández (1997)	whole year 1984		38
	France (Corsica)	Lequy et al. (2013)	December 2009 – March 2012		33
	France (Corsica)	Lequy et al. (2013)	December 2009 – March 2012	11–72	34
	France (Corsica)	Bergametti and Fôret (2014)	February 1985 – April 1986		31
	Italy (Sardinia)	Goudie and Middleton (2001)	1990 – 1995	16–36	
	Greek (Crete)	Díaz-Hernández and Miranda-Hernández (1997)	1988 – 1994	27–90	52
	Greek (Crete)	Bergametti and Fôret (2014)	1988 – 1994	30–63	
	Greek (Crete)	Goudie and Middleton (2001)	January 1988 – September 1990	27–274	
	Aegean Sea	Goudie and Middleton (2001)	1988 – 1992	31–100	
East Mediterranean sites	Turkey	Bergametti and Fôret (2014)	August 1991 – December 1992		36
	Israel (coastline)	Goudie and Middleton (2001)	February 1994, December 1994, February 1995, April 1995		197
	Israel coast (40–100 miles off the coast)	Goudie and Middleton (2001)	February 1994, December 1994, February 1995, April 1995		99
	Israel	Díaz-Hernández and Miranda-Hernández (1997)	March 1976 – February 1977	55–110	
African sites	Libya	Bergametti and Fôret (2014)	June 2000 – May 2021		332
	Sur Chad	Goudie and Middleton (2001)	1966–1967		299
	SW Niger	Goudie and Middleton (2001)	1985–1989		575
	Nigeria (North)	Díaz-Hernández and Miranda-Hernández (1997)	1976–1979	378–493	
	Gulf of Guinea	Goudie and Middleton (2001)	January – March 1988 and March – April 1990	9–32	

major and minor axis (ellipse), shape factor, aspect ratio (AR), maxferet/minferet, and roundness. The AR was calculated by fitting an ellipse to the projected particle area and dividing the major by the minor axis (Kandler et al., 2007). Roundness is defined as the ratio of four times the area by one pi times the square of the major axis ($4 \times area / \pi * major\_axis^2$). Shape factor is the ratio of the perimeter of a squared particle by four times pi times the projected area ($perimeter^2 / 4 * \pi * area$). This dimensionless parameter was used as an indicator of particle complexity. The shape factor describes how 'jagged' a particle is, by definition, equal to 1 for a circle (Reid et al., 2003).

Statistical analysis was performed using IBM SPSS Statistics (v. 22) software to perform principal component analysis and crosstabs.

2.5.4. Minor elements concentration

Minor element content (including rare earth elements [REE]) was determined by inductively coupled plasma mass spectrometry (ICP-MS) with a quadrupole ion filter NEXION 300D PERKIN-ELMER, USA (detection limits < 0.0001 mg kg^{-1}). The samples were previously disaggregated in HNO_3 and HF.

Minor element concentrations were normalised to chondrite (standard CI chondrite of McDonough and Sun, 1995). REEs were grouped as follows: light (LREE: La, Ce, Pr, Nd), medium (MREE: Sm, Eu, Gd, Tb, Dy), and heavy (HREE: Ho, Er, Tm, Yb, Lu); Y was not considered in this classification. In graphic representations, Y is placed between Ho and Er (Korotev, 2009). Geochemical indices $HREE_N/LREE_N$ and $MREE_N/LREE_N$ were calculated (Mourier et al., 2008; Laveuf and Cornu, 2009); the suffix "N" indicates that the value normalised to chondrite is used.

3. Results and discussion

3.1. PM10 concentration

PM10 concentrations between January 2012 and December 2014 fluctuated between 11 and 51 μg m^{-3} throughout the study period (Fig. 1). In the spring sampling periods (May–June), PM10 values vary between 22.00 and 25.33 μg m^{-3} (Table 1). The 16PA sample showed the lowest value. The PM10 daily legal limit (50 μg m^{-3}: European Union Directive, 2008/50/EC) was exceeded on 05/18/2012 at the Palacio de Congresos station (sampling period 4PA), on 6/06/2014 at all stations (sampling period 28PA), and on 06/11/2014 at the Ciudad Deportiva station (sampling period 28PA) (Junta de Andalucía, 2021b). These high concentrations are beyond PM10 daily legal limits and indicate a health risk (WHO, 2013b).

3.2. HYSPLIT backward trajectories

HYSPLIT backward trajectories at the Granada sampling location showed a predominant North and East Atlantic provenance similar to

Table 3
Laser Granulometry (grain size) and statistical parameters of atmospheric dust samples[1].

	16PA	28PA
Grain size (%)		
Medium and coarse sand (250–2000 μm)	0.00	5.46
Fine sand (125–250 μm)	3.57	7.51
Very fine sand (62–125 μm)	25.64	20.79
Coarse and very coarse silt (16–62 μm)	53.41	43.02
Medium silt (8–16 μm)	8.59	9.94
Very fine and fine silt (2–8 μm)	6.77	9.93
Clay < 2 μm	2.02	2.73
PM10 (<10 μm)	12.32	17.17
Statistical parameters (arithmetic; μm)		
Mean	48.25	84.16
Sorting (σ)	34.81	157.30
Skewness (*Sk*)	0.89	4.96
Kurtosis (*K*)	3.27	34.38

[1] 4PA sample quantity was insufficient to do Laser Granulometry.

that of Reche et al. (2018) (origin from the east coast of the United States or northern Europe). The influence of the African continent was lower (Fig. 2, Table 1), which is similar to other studies (Cerro et al., 2020). The 16PA sample had little influence from the African continent (6% of backward trajectories were from, or had passed through, Africa), and in 4PA and 28PA, the African influence was greater (26% and 33%, respectively). These percentages are consistent with those provided by the Ministry for Ecological Transition and Demographic Challenge (2021). Rarely, air mass circulation was observed in the Mediterranean area.

3.3. Atmospheric dust deposition rates

16PA showed the highest deposition rate (159 mg m^{-2} day^{-1}; Table 2); the 4PA and 28PA rates were lower and similar between them (114 and 108 mg m^{-2} day-^{1}, respectively; the similarity between 4PA and 28PA is noticeable but differs from 16PA, as observed in backward trajectories). The deposition rates in this study were within the ranges observed by other authors in the Granada area (Díaz-Hernández and Miranda-Hernández, 1997; Díaz-Hernández and Párraga, 2008; Díaz-Hernández et al., 2011; Morales-Baquero et al., 2013; Párraga et al., 2021) and similar to the spring period sample collected by Díaz-Hernández and Párraga (2008) (Table 2). However, deposition rates are always higher than the average bibliography rates because of the spring months (this study), which have the highest deposition rates (Díaz-Hernández et al., 2011; Torfstein et al., 2017; Cerro et al., 2020). Our deposition rates (Table 2) contrast with the mean values from 1) Spain (usually lower and similar to Gran Canaria), 2) Europe (lower), and 3) Africa (higher). Lequy et al. (2018) demonstrated a decrease in the influence of Saharan dust in European areas far from it. In addition, lower latitudes show climate dryness and an absence of vegetal cover on soils, promoting aeolian particle erosion–deposition.

3.4. Particle size distribution

The main grain size fractions in the study samples were coarse and very coarse silt (16–62 μm; 53.41% and 43.02% for 16PA and 28PA, respectively; Table 3); the clay fraction also showed low percentages (2.02% and 2.73% for 16PA and 28PA, respectively). These data were also observed by Menéndez et al. (2007; 2014) for atmospheric dust collected from the Canary Islands. The grain size < 16 μm (medium silt, very fine, and fine silt and clay) showed higher percentages in 28PA, which could indicate a greater influence of Saharan transport according to Menéndez et al. (2009) and a health problem (WHO, 2013b). The coarser fractions (sand) originate from a proximal local source.

All statistical parameters (mean, sorting, skewness, and kurtosis) showed differences between samples (Table 3). A strong positive skewness is shown in 28PA and was also observed in the Canary Islands (Menéndez et al., 2007) and Tenerife (Criado and Dorta, 2003); notably, this is evidence of suspension transport (Nickling, 1983). However, 16PA showed a skewness close to zero (Table 3).

Table 4
Mineralogy (XRD) of atmospheric dust samples.

	4PA	16PA	28PA
Phyllosilicates			
1.0–1.5 nm phyllosilicates		1	1
Illite	23	26	27
Paragonite		7	9
Chlorite	2	1	1
Kaolinite	18	23	17
Palygorskite		<1	
Total phyllosilicates	43	58	55
Tectosilicates			
Quartz	20	16	16
K-feldspar		1	2
Plagioclases	2	<1	
Total tectosilicates	22	17	18
Carbonates			
Calcite	20	12	16
Dolomite	10	4	4
Total carbonates	30	16	20
Others			
Iron oxides	tr	2	1
Amphibole			<1
Gypsum	<1		
Silvite	2	5	3
Halite	3	2	3

tr: traces.

3.5. Mineralogical composition

Mineralogy (XRD) is heterogeneous in terms of mineral species and quantities (Table 4). These minerals were detected: phyllosilicates (mainly illite followed by kaolinite and in less abundance mixed layers with reflection between 1.0 and 1.5 nm d_{001} −1.0–1.5 nm phyllosilicates-, paragonite, palygorskite, and chlorite), tectosilicates (quartz and minor contents of K-feldspar and plagioclases), carbonates (calcite and dolomite), iron oxides (hematite and goethite), amphibole, gypsum, sylvite, and halite. Total phyllosilicates were the most abundant (43%–58%), followed by total carbonates (16%–30%) and quartz (16%–20%). Calcite was at least twice the amount of dolomite. The rest of the mineral phases were a minority; some, namely, palygorskite, amphibole, or gypsum, were present in only one sample and < 1% quantities. Except for sylvite and amphibole, all mineral species detected have been described in the atmospheric dust of Granada and its metropolitan area (Díaz-Hernández and Párraga, 2008; Díaz- Hernández et al., 2011; Rodriguez-Navarro et al., 2018; Párraga et al., 2021). The presence of amphiboles is a remarkable result because of its negative impact on human health when inhaled (IARC, 2012).

In the triangle Carbonates — Tectosilicates — Phyllosilicates + Fe oxides (Fig. 3), the samples (4PA, 16PA, and 28PA) take up a small area characterised by high contents of phyllosilicates + iron oxides (43%–60%) and low and similar values of carbonates and tectosilicates. 4PA separates from 16PA and 28PA because of the lower percentage of phyllosilicates + iron oxides.

The atmospheric dust samples collected in Granada (Díaz-Hernández et al., 2011; Rodriguez-Navarro et al., 2018; Párraga et al., 2021) were similar to those of the study samples (Fig. 3). Díaz-Hernández and Párraga (2008)'s samples were separated because of their low contents of phyllosilicates and iron oxides. The quantification method must be considered to compare the mineralogical composition (XRD) (Párraga et al., 2021). However, linearity and a positive relationship between carbonates and tectosilicates ($R^2 = 0.585$ and $n = 8$; relationships not described thus far) were detected in all atmospheric dust samples collected in Granada (including those in this study).

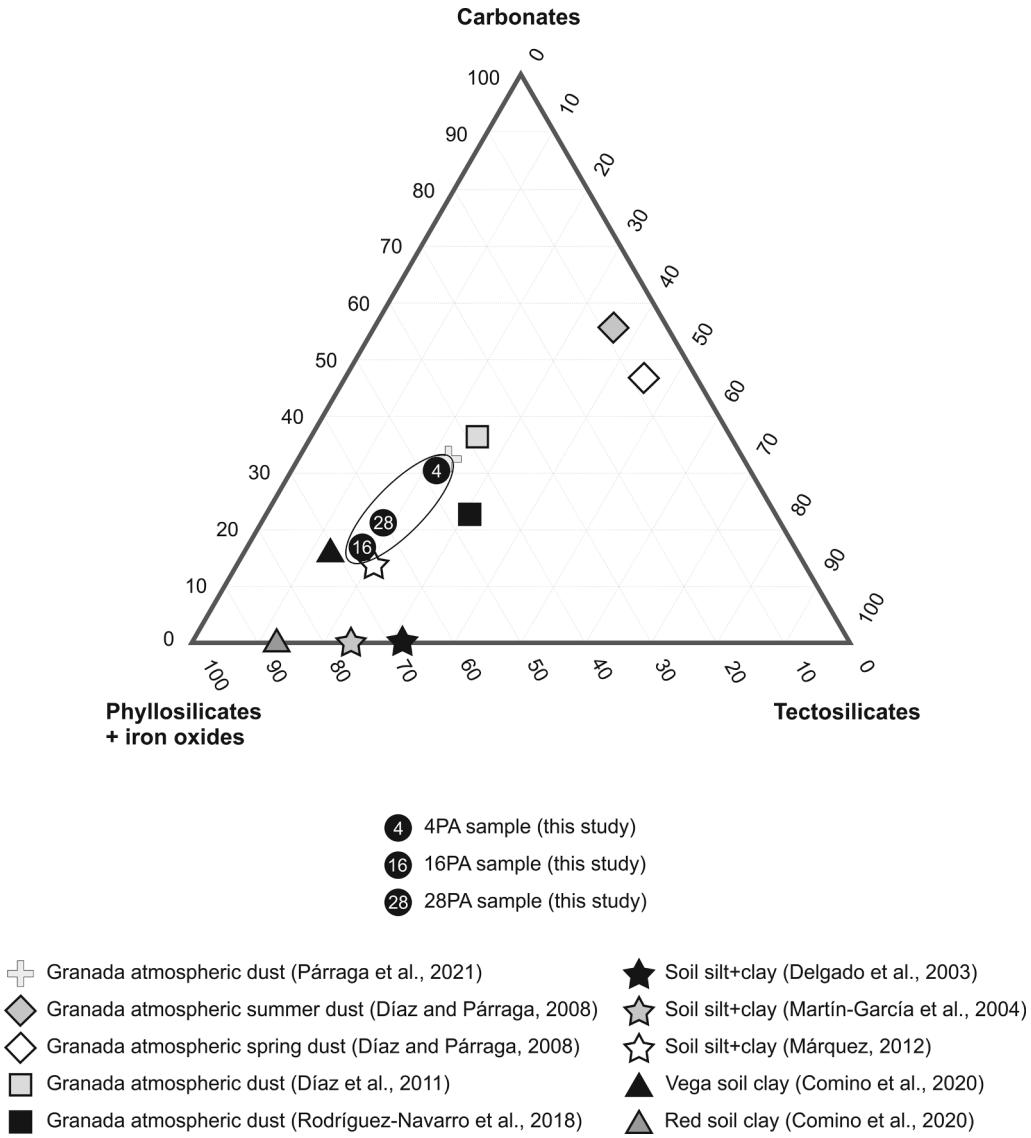

Fig. 3. Triplot Carbonates – Phyllosilicates + Iron oxides – Tectosilicates of atmospheric dust samples. The study samples are surrounded by an ellipse.

Moreover, fine fractions (<50 μm) of southern Iberian Peninsula soils (Delgado et al., 2003; Martín-García et al., 2004; Márquez, 2012; Comino et al., 2020- Vega Soil Clay; Comino et al., 2020- Red Soil Clay), a possible source of atmospheric dust, are close (but with higher contents of phyllosilicates + iron oxides) to 16PA and 28PA (Fig. 3).

3.6. *Quartz grains study*

Quartz grains observed by SEM-EDX were morphologically heterogeneous (Fig. 4). They are mainly monocrystalline (Fig. 4b, d) and some polycrystalline (Fig. 4a, c, e, f; sometimes small crystal aggregates). Well-rounded and polished grains of aeolian origin were observed (Fig. 4c). Fresh-looking subangular-angular grains, without aeolian evolution, were also found (Fig. 4b, d).

The most frequent mechanical microtextures (Table 5) were 'edge rounding' (approximately 90% of the grains; Fig. 4a,b,c,f), 'bulbous edges' (23%–50%; Fig. 4a,c,f), 'upturned plates' (14%–60%; Fig. 4a,f) and 'mechanically upturned plates' (38%–49%; Fig. 4a,f). These microtextures are typical of aeolian environments (Costa et al., 2013; Vos et al., 2014) because the impact between particles generates an amorphous silica pellicle (Fig. 4a,f). The chemical precipitation microtextures (verified by EDX) were 'silica flower' and 'silica pellicle' (Fig. 4c). The dissolution microtextures were 'corrosion gulf' and 'solution pits'. According to Baker et al. (2014), atmospheric transport alters the chemical composition of mineral particles, and pellicles can be found in aeolian grains. Geochemical activity was imprinted on the surface of the grains. The 'solution pits' microtextures detected in 16PA (33%) are associated with inheritance from pedological processes (Vos et al., 2014). Medium relief was dominant in this study, followed by low and high relief. According to Vos et al. (2014), low relief is the most abundant in aeolian environments, followed by medium relief.

The chi-square $\chi 2$ statistical study showed significant differences between samples for 'bulbous edges' ($P < 0.05$), 'upturned plates' ($P < 0.001$), and 'solution pits' ($P < 0.001$). The first two are characteristics of aeolian environments, and their occurrence frequencies are higher in 4PA and 28PA (Table 5). Solution pits are characteristic of pedogenic environments, and 16PA has the highest occurrence frequency (Table 5), further proof of the two sample groups.

Quartz grain shape parameters corroborate the differences between samples (4PA and 28PA similar and different from 16PA; Table 6). Differences were notable for area, perimeter, maxferet, minferet, maxferet/minferet, major axis (ellipse), and minor axis (ellipse) parameters (Table 6). AR values were consistently higher than 1, and 16PÁs shape factor parameter shows the highest value,

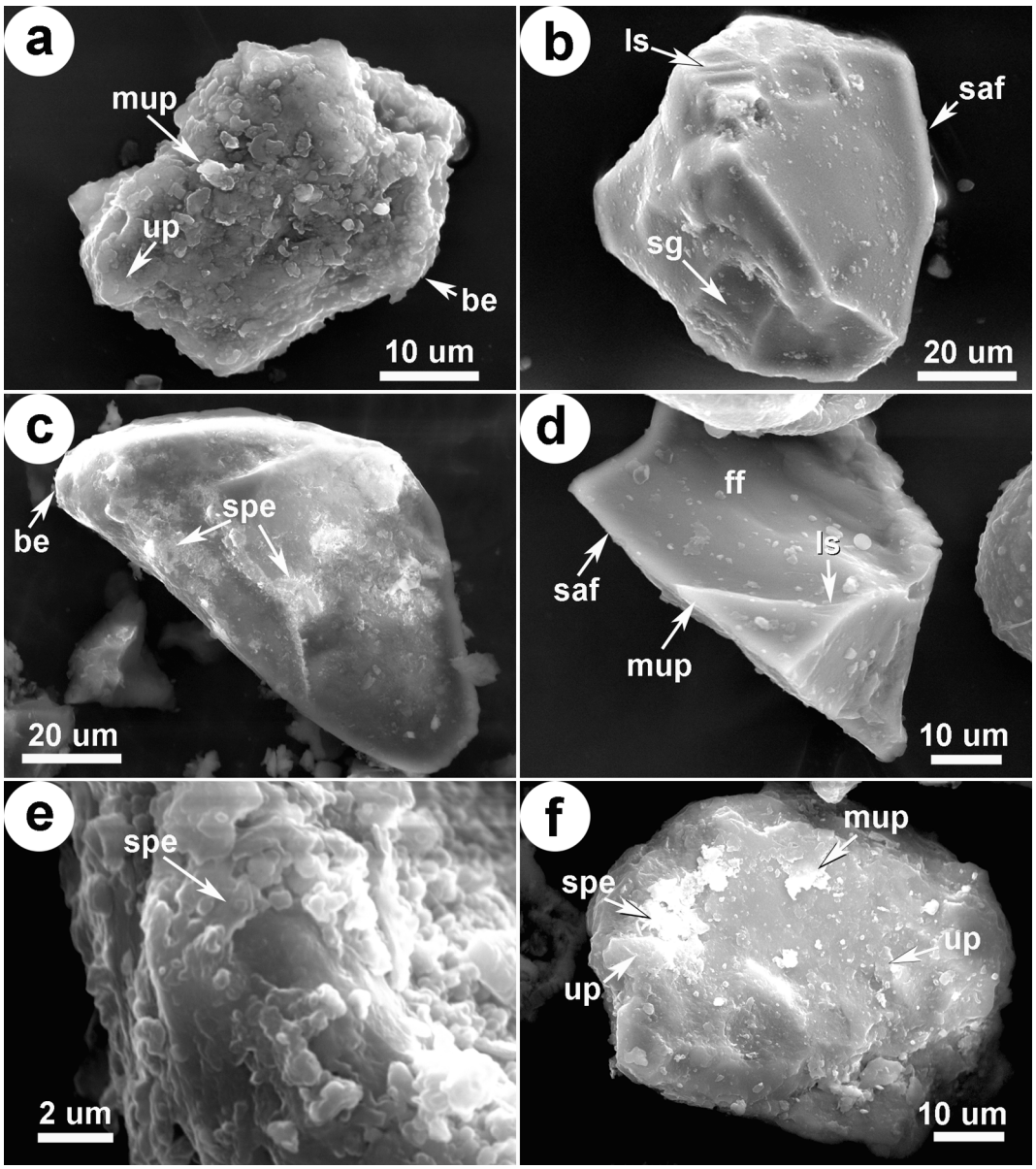

Fig. 4. SEM images of quartz grains: a) 4PA sample. Medium relief polycrystalline grain (43 μm maximum diameter), subrounded, whit typical aeolian microtextures, namely, upturned plates (up), bulbous edges (be), and mechanically upturned plates (mup); b) 4PA sample. Medium relief monocrystalline grain (59 μm long) in which crystal faces are recognised. Clear surface, subrounded perimeter with mechanical microtextures, namely, sharp angular features (saf), linear steps (ls), and straight grooves (sg); c) 16PA sample. Low relief polycrystalline grain (102 μm long). Typical aeolian microtextures, namely, rounding, bulbous edges (be), silica pellicle (spe), and polished surface, are observed; d) 4PA sample. Low relief monocrystalline grain (59 μm long). Mechanical microtextures, namely, saf, mup, ls, and fracture face (ff), are observed. All these mechanical microtextures denote a fresh-looking aspect (little aeolian evolution); e) 28PA sample. Enlargement of a surface quartz grain showing silica pellicle (spe); f) 28PA sample. Low relief polycrystalline grain (63 μm long) showing silica pellicle (spe) and typical mechanical aeolian microtextures, namely, upturned plates (up) and mechanically upturned plates (mup).

indicating a greater irregularity of its particles, according to Reid et al. (2003).

Principal component analysis of the shape parameters found two components (PC1 and PC2), which explained 91.20% of the sample variability. Again, 16PA differed from 4PA and 28PA (Fig. 5). The PC1 component collects parameters related to quartz grain size (area, perimeter, maxferet, minferet, major axis, minor axis), which differentiates 16PA from 4PA and 28PA.

3.7. Minor elements composition

Zn, Sr, Ba, Mn, and Cr were the most abundant minor elements (>100 ppm in at least one of the three samples studied; Table 7). 16PA always shows the lowest values (except for Mo, Cd, Sn, Sb, and Pb) and differs from 4PA and 28PA (similar in most cases). These results are consistent with the trends already observed. The samples showed high content of Pb and Sr compared with that in the bibliography data (Scheuvens et al., 2013).

Fig. 6 shows the two groups of samples. 4PA and 28PA are almost coincident and parallel to 16PA, except for Pb, Th, and As.

Additionally, REE composition presents the following characteristics (Table 8): 1) REEs follow the Earth's crust abundance order (Ce > La > Nd > Y > Pr > Sm > Gd > Dy > Er > Yb > Eu > Ho > Tb > Tm > Lu); however, there are exceptions in the HREE, where the order changed between some contiguous elements (Lu > Tm sample 28PA; Tb > Ho sample 4PA; Yb > Er sample 4PA and 16PA). 2) LREEs are the most

Table 5
Occurrence frequency (%) of quartz microtextures[1] from atmospheric dust samples.

	4PA	16PA	28PA		4PA	16PA	28PA
Mechanical				Mechanical			
Edge rounding	92	88	90	Bulbous edges	36	23	50
Sharp angular features	22	32	12	Upturned plates	60	14	48
Conchoidal fractures	4	2	2	Subparallel linear fractures	4	2	0
Arc-shaped steps	6	9	0	Chemical			
Linear steps	6	4	8	Solution pits	0	33	2
Fracture faces	8	16	4	Corrosion gulf	30	18	12
V-shaped percussion cracks	4	2	2	Silica flowers	20	11	23
Breakage blocks	6	4	6	Silica pellicle	14	21	17
Straight grooves	6	9	6	Combined mechanical and chemical			
Curved grooves	4	2	2	Low relief	36	21	40
Mecanically upturned plates	48	49	38	Medium relief	52	67	46
				High relief	10	12	13

[1] According to Mahaney (2002), Vos et al. (2014) and Sweet and Brannan (2016).

Table 6
Shape parameters obtained by Image Analysis (IA) from SEM quartźs micrographs.

	4PA (n = 49)		16PA (n = 56)		28PA (n = 51)	
	Mean	SD	Mean	SD	Mean	SD
Area (μm^2)	1253.78	707.88	3495.99	2119.16	1037.04	697.66
Perimeter (μm)	154.49	43.41	269.97	92.29	141.31	50.02
Maximum Feret (μm)	50.08	13.98	81.92	28.82	45.23	16.02
Minimum Feret (μm)	33.53	10.89	57.04	18.27	29.52	11.26
Maximum Feret / Minimum Feret	1.55	0.34	1.46	0.31	1.60	0.44
Major axis (μm)	47.21	12.85	76.53	27.70	42.82	15.17
Minor axis (μm)	31.74	10.40	53.77	17.24	28.06	10.77
Shape Factor	1.66	0.33	1.81	0.31	1.73	0.30
Aspect Ratio	1.56	0.41	1.45	0.36	1.61	0.51
Roundness	0.68	0.14	0.72	0.14	0.67	0.17

SD, Standar deviation.

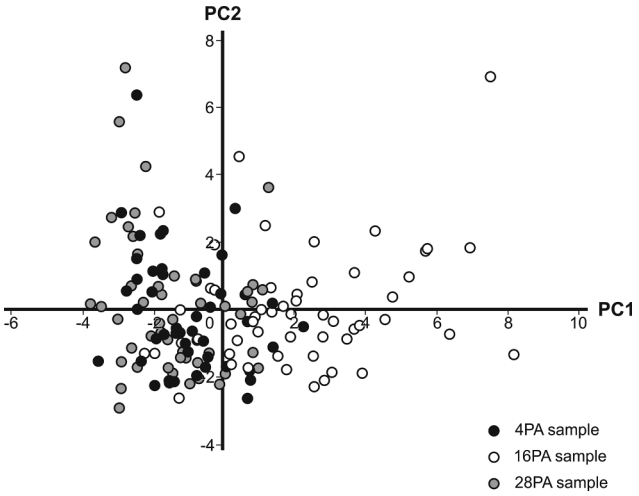

Fig. 5. Principal component analysis biplot (PC1 *vs*. PC2).

abundant, followed by MREE and HREE. 3) 16PA has lower ∑REE than 4PA and 28PA (which present similar values), confirming the existence of two groups again. 4) The normalised chondrite profiles show (Fig. 7) 4.1) normalised values that are always higher than 1 (amounts higher than reference meteorite), except for Lu (0.98) in 16PA. This sample shows exceptionally low values, close to 1 in several elements (Fig. 7); 4.2) enrichment in LREE, demonstrated by a strong negative slope (with atomic number growth), which decreases from Eu and becomes flatter in the HREE. This is shown by the $MREE_N/LREE_N$ (0.14 to 0.17) and $HREE_N/LREE_N$ (0.11 and 0.14) ratio values (Table 8); 4.3) the study samples have a noticeable negative europium anomaly. In addition, the positive anomalies of erbium (28PA), ytterbium (4PA, 16PA, and 28PA), and yttrium (16PA) are perceptible (Fig. 7).

We compared this study of REE contents with the literature (Table 8 and Fig. 7) and the following was observed: 1) Lower ΣREE in this studýs samples because they have a coarser grain size (Table 3) than SSH (silt size), LE (5–20 μm), and AD (<20 μm). This finding supports that of Xie et al. (2014), that is, grain size exerts an evident influence on REE compositions. Thus, REE are concentrated in the silt (2 to 50 μm) and clay (<2 μm) fine fractions (Prudêncio et al., 1993; Aide and Smith-Aide, 2003; Marques et al., 2011). Granada dust (GD, Párraga et al., 2021) has the closest ΣREE to this study's samples because the two have a similar grain size (fine sand). 2) European soil, Spanish soil (SS), and continental crust (EC1 and EC2) normalised chondrite profiles are closer to our study's samples than the materials from Africa (Fig. 7). 3) Our samples' $HREE_N/LREE_N$ and $MREE_N/LREE_N$ ratio values are generally lower than those in literature; the exceptions are GD (0.12) and SS (0.13) for $HREE_N/LREE_N$ and SS (0.17) for $MREE_N/LREE_N$ (Table 8).

3.8. *Provenance fingerprints of atmospheric dust. Quartz evidence*

The results obtained can be regarded as atmospheric dust provenance fingerprints.

4PA and 28PA showed the highest backward trajectory percentages from North Africa, the highest PM10 concentrations (expressed in μg m^{-3} and as a percentage), and the lowest deposition rates (Tables 1, 2, and 3). However, 16PA shows the lowest backward trajectory percentage from Africa, the lowest PM10 concentration, and the highest deposition rate. These results indicates a greater Sahara Desert influence on 4PA and 28PA. The decrease in deposition rates when PM10 increases could be due to the inefficiency of removal processes of small-diameter particles (<2.5 μm) (Bergametti and Forêt, 2014), allowing them to remain suspended in the atmosphere for longer and enabling long-distance travel. However, large particles (mainly > 10 μm) settle

Table 7
Minor elements (ppm) of atmospheric dust samples.

	4PA	16PA	28PA		4PA	16PA	28PA		4PA	16PA	28PA
Be	0.50	0.10	0.77	Mo	1.95	1.97	4.01	U	0.81	0.45	1.00
Sc	2.28	1.04	4.06	Cd	0.13	0.14	0.60	Li	9.18	5.51	16.48
V	28.88	13.49	35.48	In	0.09	0.07	0.08	Rb	24.27	14.94	37.52
Cr	33.27	22.60	106.80	Sn	12.07	15.02	7.90	Cs	1.49	0.78	2.03
Mn	148.52	85.87	239.20	Sb	18.89	11.95	11.52	Sr	318.79	155.10	357.58
Co	12.19	8.98	20.96	Ba	201.13	90.34	170.49	Ga	4.36	2.21	6.59
Ni	17.29	15.23	57.07	Tl	0.16	0.08	0.20	Nb	2.51	1.90	7.88
Cu	84.18	58.48	70.79	Pb	36.06	74.79	32.39	Ta	0.11	0.01	0.41
Zn	410.30	247.62	319.97	Bi	0.51	0.36	0.43	Zr	11.70	10.75	52.18
As	3.49	0.61	3.79	Th	3.48	1.20	4.62	Hf	0.42	0.33	1.32

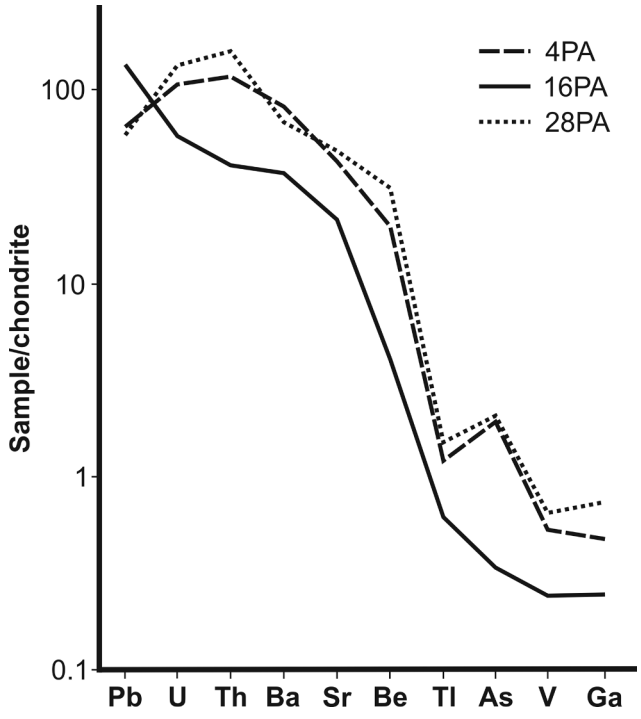

Fig. 6. Chondrite normalised diagram of selected minor elements.

quickly (Bergametti and Forêt, 2014), which suggests a local origin. The weak correlation of PM10 and dust deposition rates may be also caused by the wet and dry deposition events differences of the studied period. Besides, the urban and rural pollution, a main component of the PM10 fraction, could contribute to this poor correlation (Querol et al., 2001; Rodríguez et al., 2011).

The greater abundance of quartz microtextures, namely, bulbous edges and upturned plates (Table 5), prints a greater aeolian character to 4PA and 28PA (Costa et al., 2013). By contrast, the presence of solution pits in 16PA quartz grains indicates a greater participation of local origin. Martín-García et al. (2004, 2015) discovered solution pits microtexture in quartz from southern Spain soils.

Quartz grain shape parameters (Table 6, Fig. 5) indicate the differences between the samples. The lower PC1 values (in principal component analysis) for the 4PA and 28PA samples (Fig. 5) show a smaller area, perimeter, maxferet, minferet, major axis, minor axis. The atmospheric dust AR values provided by Scheuven and Kandler (2014) for atmospheric dust from Africa varied between 1.57 and 1.90, consistent with the 4PA (1.56) and 28PA (1.61) values. However, 16PA was outside the range (1.45). The quartz grain AR values provided by Kandler et al. (2007) for African dust collected in Tenerife (Spain) were 1.60, remarkably close to 4PA (1.56) and 28PA (1.61) (Table 6). All previous results support a greater African influence on 4PA and 28PA. According to Coz (2008), the highest AR values correspond to greater transport distances, suggesting that 4PA and 28PA can undergo greater atmospheric transport than 16PA. For quartz grains, the shape factor, 4PA (1.66), and 28PA (1.73) values (Table 6) are within the African dust range (1.53–1.76) provided by Chou et al. (2008); 16PA would be out of the range (1.81).

The XRD mineralogy (Table 4) allows us to interpret the African origin of atmospheric dust by Scheuvens et al. (2013)'s indices (Table 9). In this manner, 4PA and 28PA could be influenced by the Libya central zone (PSA4) because they have illite/kaolinite between 0.2 and 1.9, chlorite/kaolinite between 0.0 and 2.6, carbonate content (calcite + dolomite) from low to intermediate (1%–30%), and palygorskite absence. However, 16PA could be influenced by African dust from Libya (PSA4), southern Algeria, northern Mali (PSA3), and the foothills of the Atlas mountains and the western coastal region (PSA2). Applying the indices of Scheuvens et al. (2013) to other atmospheric dust collected in Granada, these would show influence from 1) those of Párraga et al. (2021) from the foothills of the Atlas mountains and western coastal region (PSA2) (although with an absence of palygorskite); 2) those of Rodriguez-Navarro et al. (2018) from the foothills of the Atlas mountains and western coastal region (PSA2) (except for Ch/Ka index); 3) those of Díaz-Hernández and Párraga (2008), summer and spring samples, both from the foothills of the Atlas mountains and western coastal region (PSA2) and from western Chad including the Bodélé depression (PSA5); and 4) those of Díaz-Hernández et al. (2011) from southern Algeria and northern Mali (PSA3). The application of the Scheuvens et al. (2013) indices reveals that atmospheric dust samples from Granada (including those in this study) are not homogeneous in terms of influence from the African continent.

Furthermore, XRD mineralogy (Table 4) demonstrates that minority mineral species provide valuable information on the genesis and origin of atmospheric dust: 1) amphibole was detected in 28PA (minimal quantities). Amphibole presence is noticeable due to its genesis and implications for human health, which are remarkably notable (IARC, 2012). This mineral has not been described in African atmospheric dust samples (Scheuvens et al., 2013). However, it has been described (in few studies) in Spanish atmospheric dust and was associated with local pollution from natural sources (Menéndez et al., 2007) and with anthropogenic pollution from road traffic (wear of brake pads or clutch discs) (Amato et al., 2011). Jeong (2008) and Lequy et al. (2013) have detected amphiboles in Asian and northern French atmospheric dust, respectively. The authors concluded that amphiboles originated from local soils. In this study, amphiboles in 28PA could be due to local anthropic contamination from construction materials (e.g. corrugated fibre

Table 8
Rare earth elements content (ppm) and selected geochemical ratios in atmospheric dust samples and other materials from bibliography.

	This study			Other materials[1]							
	4PA	16PA	28PA	SSH	LE	GD	AD	EC1	EC2	SS	ES
La	8.49	3.64	12.82	44.33	25.81	14.56	50.05	31.00	30.00	38.83	25.86
Ce	19.32	7.06	26.51	95.44	53.27	29.49	105.53	63.00	64.00	81.27	52.25
Pr	2.12	0.81	2.92	10.89	6.57	3.31		7.10	7.10	9.80	6.02
Nd	7.07	3.17	10.38	47.44	25.81	12.05	48.85	27.00	26.00	34.96	22.41
Sm	1.46	0.61	2.21	7.22	4.97	2.34	9.63	4.70	4.50	6.49	4.28
Eu	0.22	0.07	0.36	1.22	1.03	0.51	1.93	1.00	0.88	1.12	0.85
Gd	1.23	0.46	1.82	8.67	4.47	1.90	10.07	4.00	3.80	5.40	4.20
Tb	0.15	0.05	0.21	1.11	0.67	0.26	1.26	0.70	0.64	0.71	0.64
Dy	0.76	0.27	1.24	7.33	4.46	1.46		3.90	3.50	3.91	3.58
Ho	0.13	0.06	0.24	1.33	0.97	0.26	1.64	0.83	0.80	0.73	0.72
Y	3.47	1.83	5.84	25.11	27.99	7.38		21.00	22.00	20.01	
Er	0.38	0.17	0.83	3.44	2.84	0.67		2.30	2.30	2.01	2.10
Tm	0.06	0.03	0.09	0.75	0.47	0.09		0.30	0.33	0.29	0.31
Yb	0.41	0.25	0.65	3.78	2.96	0.61	4.32	1.96	2.20	1.85	2.09
Lu	0.04	0.02	0.09	0.67	0.46	0.10	0.63	0.31	0.32	0.27	0.31
∑REE	41.83	16.66	60.37	233.64	134.75	67.61	233.91	148.10	146.37	187.64	125.62
∑LREE	37.00	14.68	52.63	198.11	111.46	59.41	204.43	128.10	127.10	164.86	106.54
∑MREE	3.82	1.45	5.84	25.56	15.60	6.48	22.89	14.30	13.32	17.63	13.56
∑HREE	1.01	0.53	1.89	9.97	7.69	1.72	6.59	5.70	5.95	5.15	5.52
$HREE_N/LREE_N$	0.11	0.13	0.14	0.22	0.28	0.12	0.17	0.18	0.19	0.13	0.21
$MREE_N/LREE_N$	0.16	0.14	0.17	0.22	0.24	0.19	0.24	0.20	0.18	0.17	0.22

[1] SSH, Sahara-Sahel corridor (Moreno et al., 2006); Libya-Egypt materials (Abed et al., 2009); GD, Granada dust (Párraga et al., 2021); AD, African dust (Muhs et al., 2010); EC1, mean composition of continental crust (Rudnick and Gao, 2003); EC2, mean composition of continental crust (Taylor and McLennan, 1985); SS, Spanish top soil (Locutura et al., 2012); ES, European top soil (Salminen et al., 2005).

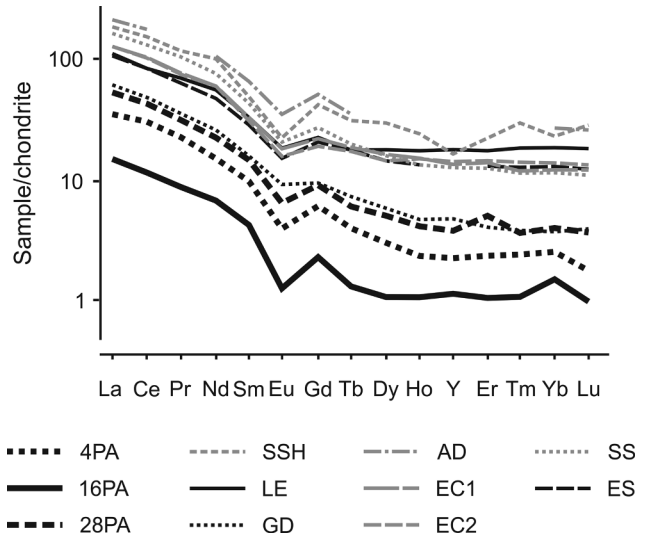

Fig. 7. Chondrite normalisation of REE contents of atmospheric dust samples and other materials from the bibliography. See Table 8 for abbreviation explanations.

cement roofing) and dust from the traffic of urban areas (Amato et al., 2011); 2) gypsum, detected in 4PA, described both in atmospheric dust from the Sahara (Scheuvens et al., 2013) and neo-formed in the atmosphere from the weathering of other minerals (Díaz-Hernández and Párraga, 2008); 3) sylvite, detected in all samples and reported for the first time, according to our review of the literature, in atmospheric dust collected in Granada, which may have a natural origin associated with the erosion of sylvite-bearing rocks and soils present in the Granada Basin (SE Spain) (López-Quirós et al., 2016), or an origin associated with marine aerosols (Blondet et al., 2019); 4) palygorskite, already described in Granada (Díaz-Hernández et al., 2011; Rodriguez-Navarro et al., 2018) and only detected in 16PA, indicates a potential source from Tunisia and northern Algeria (including the 'zone of chotts' [PSA1]), the foothills of the Atlas mountains and western coastal region (PSA2) or southern Algeria and northern Mali (PSA3) (Scheuvens et al., 2013); 5) paragonite, detected in 16PA and 28PA, is an abundant mineral in geological materials from southern Spain (Martin-Garcia et al., 1997) and in Rif's materials from Morocco (Rodríguez-Ruiz et al., 2019) and has been described in Granada atmospheric dust (Díaz-Hernández et al., 2011; Párraga et al., 2021). Paragonite presence could indicate an influence from northern Africa (Morocco) and south of the Iberian Peninsula.

Moreover, mineralogical similarities (Fig. 3) between atmospheric dust and soil fine fractions from the south of the Iberian Peninsula could be a provenance indication. 16PA is the closest (in the mineralogical triangle) to the soil samples (higher phyllosilicates + iron oxides content). Atmospheric dust samples located far from soil samples (Fig. 3) show more phyllosilicates + iron oxides and fewer carbonates + tectosilicates. This finding could indicate that local soils contribute as the main focus of phyllosilicates + iron oxides, and carbonates + tectosilicates could be from a different source.

Geochemistry can also provide evidence for provenance. Once again, the two groups differ: 16PA (usually lower contents) differs from 4PA and 28PA (Tables 7 and 8, Figs. 6 and 7).

In this study, the samples showed higher Pb and Sr contents than those of most atmospheric dust from the Scheuvens et al. (2013) database: Sr is only surpassed in one case (by dust deposited in the Azores), and Pb is only exceeded in 7% of database cases (by dust collected in Italy and Beirut/Lebanon). The relatively high Sr contents can be explained by the proximity to Montevives and Escúzar, celestine mines ($SrSO_4$) located 20 km from Granada city. The relatively high Pb values must be attributed to anthropogenic influence (road traffic) (Parviainen et al., 2020), indicating a local influence on the study samples.

The ∑REE in this study showed values lower than those in the bibliography materials (Table 8, Fig. 7). The lower ∑REE content, as discussed, is due to the higher particle sizes. Thus, the ∑REE content in

Table 9
Mineralogical indices (and Saharan provenance) of atmospheric dust samples.

Sample	Reference	Type of event	Date/Period/Year of event	Il/Ka	Ch/Ka	Palygorskite (%)	Carbonates (%)	Ca/Do
4PA	This study	DD + WD	26-April to 31-May 2012	1.28 (1,3,4)	0.11 (2,4)	nd (4,5,6)	30 (1,2,3,4)	2
16PA	This study	DD + WD	10-May to 13-June 2013	1.13 (1,3,4)	0.04 (2,4)	<1 (1,2,3)	16 (1,2,3,4)	3
28PA	This study	DD + WD	16-May to 18-June 2014	1.59 (1,4)	0.06 (2,4)	nd (4,5,6)	20 (1,2,3,4)	4
Atmospheric dust samples from Granada								
	Díaz-Hernández and Párraga (2008)	DD	sumer 2001, 2002 and 2004	2.25 (2)	(5)	nd (4,5,6)	52 (1,2,3)	0.23
		DD	1- to 2-April 2005	3.00 (2)	(5)	nd (4,5,6)	46 (1,2,3)	0.07
	Díaz-Hernández et al. (2011)	DD	whole year 1992	0.89 (3,4)	0.46 (2,3,4)	tr (1,2,3)	26 (1,2,3,4)	0.91
		DD	whole year 1992	1.06 (1,3,4)	0.46 (2,3,4)	tr (1,2,3)	30 (1,2,3,4)	0.61
		DD	whole year 1992	0.33 (3,4,5)	0.38 (2,3,4)	tr (1,2,3)	22 (1,2,3,4)	2.65
	Rodríguez-Navarro et al. (2018)	RR	21 to 23 February 2017	3.36 (2)	(5)	11 (1,2)	23 (1,2,3,4)	4.50
	Párraga et al. (2021)	DD	June to October 2010	4.25 (2)	0.38 (2,3,4)	nd (4,5,6)	32 (1,2,3)	0.58

Abbreviations: Il, illite; Ka, kaolinite; Ch, Chlorite; Ca, calcite; Do, dolomite; DD, dry deposition; WD, wet deposition; RR, red rain; nd, non-detected; tr, traces. Source areas according to Scheuvens et al. (2013): (1) PSA1, Tunisia and northern Algeria including the 'zone of chotts'; (2) PSA2, Foothills of Atlas mountains and western coastal region; (3) PSA3, Southern Algeria and northern Mali; (4) PSA4, Central Libya; (5) PSA5, Western Chad including the Bodélé depression; (6) PSA6, Southern Egypt, northern Sudan.

atmospheric dust, linked to its grain size, can be an indicator of the transport distance.

4. Conclusions

A multitechnical study has enabled characterisation of the spring atmospheric dust (2012–2014) in Granada's strategic area (frontier of the European continent with Africa). PM10 concentration, deposition rates, grain size, XRD mineralogy, SEM quartz microtextures, SEM-IA quartz shape parameters, and minor element contents (including REE) showed differences among spring sampling periods, possibly due to differences in their provenance.

African influence has been shown by the following properties of atmospheric dust: a) apparently greater contents of PM10; b) greater presence of microtextures, namely, bulbous edges and upturned plates, on the surface of quartz grains; and c) for quartźs shape parameters, minor values for area, perimeter, maximum feret, minimum feret, major axis, minor axis, and shape factor, and higher values for AR.

The mineralogy has confirmed different origins for atmospheric dust collected in Granada: the Northwest African continent (e.g. presence of palygorskite has been described in Tunisia, Algeria, Atlas mountains, western coastal region, and northern Mali), local sources, and minerals crystallised in the atmosphere during dust transport (sylvite and gypsum). Geochemistry has evinced a local influence through the relatively high Sr and Pb contents attributable to celestine mines ($SrSO_4$) located close to Granada city and pollution from road traffic, respectively. The low $\sum$REE content in the 16PA sample is an indicator of the short distance travelled.

In summary, the applied techniques can be used as provenance fingerprints. Quartz particle morphoscopy has been revealed as a new technique for understanding atmospheric dust provenance.

Declaration of Competing Interest

The authors declare that they have no known competing financial interests or personal relationships that could have appeared to influence the work reported in this paper.

Acknowledgments

This work was supported by a grant from Ministerio de Economía, Industria y Competitividad de España ("Mediterranean Soil Typologies versus Quartz. At the frontier of pedogenic knowledge"; Ref. CGL2016-80308-P). Funding for open access charge: Universidad de Granada / CBUA.

References

Abramoff, M.D., Magalhaes, P.J., Ram, S.J., 2004. Image Processing with ImageJ. Biophotonics Int. 11 (7), 36–42.
AEMET, 2020. Estadísticos básicos climatológicos del periodo 1981–2010. Agencia Estatal de Meteorología, Ministerio de Transición Ecológica y el Reto Demográfico. Retrieved from: http://www.aemet.es/es/serviciosclimaticos/datosclimatologicos.
Aide, M., Smith-Aide, C., 2003. Assessing soil genesis by rare-earth elemental analysis. Soil Sci. Soc. Am. J. 67 (5), 1470–1476.
Amato, F., Pandolfi, M., Moreno, T., Furger, M., Pey, J., Alastuey, A., Bukowiecki, N., Prevot, A.S.H., Baltensperger, U., Querol, X., 2011. Sources and variability of inhalable road dust particles in three European cities. Atmos. Environ. 45 (37), 6777–6787.
Avila, A., Queralt-Mitjans, I., Alarcón, M., 1997. Mineralogical composition of African dust delivered by red rains over northeastern Spain. J. Geophys. Res. [Atmos.] 102 (D18), 21977–21996.
Baker, A.R., Laskina, O., Grassian, V.H., 2014. Processing and Ageing in the Atmosphere. In: Knippertz, P., Stuut, J.B. (Eds.), Mineral Dust. Springer, Dordrecht, pp. 75–92.
Barahona, E., 1974. Arcilla de ladrillería de la provincial de Granada. Evaluación de algunos ensayos de materias primas (Doctoral dissertation). Universidad de Granada, Granada.
Bergametti, G., Forêt, G., 2014. Dust Deposition. In: Knippertz, P., Stuut, J.B. (Eds.), Mineral Dust. Springer, Dordrecht, pp. 179–200.
Blondet, I., Schreck, E., Viers, J., Casas, S., Jubany, I., Bahí, N., Zouiten, C., Dufréchou, G., Freydier, R., Galy-Lacaux, C., Martínez-Martínez, S., Faz, A., Soriano-Disla, M., Acosta, J.A., Darrozes, J., 2019. Atmospheric dust characterisation in the mining district of Cartagena-La Unión, Spain: air quality and health risks assessment. Sci. Total Environ. 693, 133496. https://doi.org/10.1016/j.scitotenv.2019.07.302.
Blott, S.J., Pye, K., 2001. GRADISTAT: a grain size distribution and statistics package for the analysis of unconsolidated sediments. Earth Surf. Process. Landf. 26 (11), 1237–1248.
Calero, J., Delgado, R., Delgado, G., Martín-García, J.M., 2009. SEM image analysis in the study of a soil chronosequence on fluvial terraces of the middle Guadalquivir (southern Spain). Eur. J. Soil Sci. 60 (3), 465–480.
Candeias, C., Vicente, E., Tomé, M., Rocha, F., Ávila, P., Alves, C., 2020. Geochemical, mineralogical and morphological characterisation of road dust and associated health risks. Int. J. Environ. Res. Public Health 17 (5), 1563.
Chou, C., Formenti, P., Maille, M., Ausset, P., Helas, G., Harrison, M., Osborne, S., 2008. Size distribution, shape, and composition of mineral dust aerosols collected during the African Monsoon Multidisciplinary Analysis Special Observation Period 0: Dust and Biomass-Burning Experiment field campaign in Niger, January 2006. J. Geophys. Res. Atmos. 113, D00C10.
Cerro, J.C., Cerdá, V., Caballero, S., Bujosa, C., Alastuey, A., Querol, X., Pey, J., 2020. Chemistry of dry and wet atmospheric deposition over the Balearic Islands, NW Mediterranean: Source apportionment and African dust areas. Sci. Total Environ. https://doi.org/10.1016/j.scitotenv.2020.141187.
Comino, F., Cervera-Mata, A., Aranda, V., Martín-García, J.M., Delgado, G., 2020. Short-term impact of spent coffee grounds over soil organic matter composition and stability in two contrasted Mediterranean agricultural soils. J. Soils Sediments 20 (3), 1182–1198.
Costa, P.J.M., Andrade, C., Mahaney, W.C., Marques da Silva, F., Freire, P., Freitas, M.C., Janardo, C., Oliveira, M.A., Silva, T., Lopes, V., 2013. Aeolian microtextures in silica spheres induced in a wind tunnel experiment: Comparison with aeolian quartz. Geomorphology 180-181, 120–129.
Coz, E., 2008. Caracterización química y morfológica del aerosol ambiental en las fracciones PM10 y PM2.5 mediante microscopía electrónica de barrido en episodios. Universidad Carlos III, Madrid de contaminación atmosférica de origen diverso (Doctoral dissertation).
Criado, C., Dorta, P., 2003. An unusual "blood rain'' over the The Canary Islands (Spain). The storm of January 1999. J. Arid Environ. 55, 765–783.

Delgado, R., Barahona, E., Huertas, F., Linares, J., 1982. Los Mollisoles de la Cuenca Alta del Río Dílar Sierra Nevada. Anales de Edafología y Agrobiología 41, 59–82.
Delgado, R., Martín-García, J.M., Oyonarte, C., Delgado, G., 2003. Genesis of the terrae rossae of the Sierra Gádor (Andalusia, Spain). Eur. J. Soil Sci. 54 (1), 1–16.
Díaz-Hernández, J., Miranda-Hernández, J., 1997. Tasas de deposición de polvo atmosférico en un área semiárida del entorno Mediterráneo occidental. Estud. Geol. 53 (5–6), 211–220.
Díaz-Hernández, J.L., Martín-Ramos, J.D., López-Galindo, A., 2011. Quantitative analysis of mineral phases in atmospheric dust deposited in the South-Eastern Iberian Peninsula. Atmos. Environ. 45 (18), 3015–3024.
Díaz-Hernández, J.L., Párraga, J., 2008. The nature and tropospheric formation of iberulites: pinkish mineral microspherulites. Geochim. Cosmochim. Acta 72 (15), 3883–3906.
Draxler, R.R., 2011. HYSPLIT Model (HYbrid Single-Particle Lagrangian Integrated Trajectory). Retrieved from. https://www.ready.noaa.gov/HYSPLIT.php.
Drees, L.R., Wilding, L.P., Smeck, N.E., Senkayi, A.L., 1989. Silica in soils: quartz and disordered silica polymorphs. In: Dixon, J.B., Weed, S.B. (Eds.), Minerals in Soil Environments. Soil Science Society of America, Madison, WI, pp. 913–965.
Engelbrecht, J.P., Menéndez, I., Derbyshire, E., 2014. Sources of PM2. 5 impacting on gran Canaria. Spain. Catena 117, 119–132.
Engelbrecht, J.P., Moosmüller, H., Pincock, S., Jayanty, R.K.M., Lersch, T., Casuccio, G., 2016. Technical note: Mineralogical, chemical, morphological, and optical interrelationships of mineral dust re-suspensions. Atmos. Chem. Phys. 16 (17), 10809–10830.
European Union Directive, 2008. 50/EC of the European Parliament and the Council of 21 May 2008. Relating to ambient air quality and cleaner air for Europe. OJ L 152, 11.6.2008, pp. 1–44.
Gelado-Caballero, M.D., López-García, P., Prieto, S., Patey, M.D., Collado, C., Hérnández-Brito, J.J., 2012. Long-term aerosol measurements in Gran Canaria, Canary Islands: Particle concentration, sources and elemental composition. J. Geophys. Res. [Atmos.] 117 (D3), n/a–n/a.
Goudie, A.S., Middleton, N.J., 2001. Saharan dust storms: nature and consequences. Earth-Sci. Rev. 56 (1-4), 179–204.
Hojati, S., Khademi, H., Faz Cano, A., Landi, A., 2012. Characteristics of dust deposited along a transect between central Iran and the Zagros Mountains. Catena 88 (1), 27–36.
Huneeus, N., Schulz, M., Balkanski, Y., Griesfeller, J., Prospero, J., Kinne, S., Bauer, S., Boucher, O., Chin, M., Dentener, F., Diehl, T., Easter, R., Fillmore, D., Ghan, S., Ginoux, P., Grini, A., Horowitz, L., Koch, D., Krol, M.C., Landing, W., Liu, X., Mahowald, N., Miller, R., Morcrette, J.-J., Myhre, G., Penner, J., Perlwitz, J., Stier, P., Takemura, T., Zender, C.S., 2011. Global dust model intercomparison in AeroCom phase I. Atmos. Chem. Phys. 11 (15), 7781–7816.
IARC, 2012. Working Group on the Evaluation of Carcinogenic Risks to Humans. Arsenic, Metals, Fibres and Dusts. Lyon (FR): International Agency for Research on Cancer (IARC) Monographs on the Evaluation of Carcinogenic Risks to Humans, No. 100C. Asbestos (chrysotile, amosite, crocidolite, tremolite, actinolite and anthophyllite). Retrieved from: https://www.ncbi.nlm.nih.gov/books/NBK304374/.
Jeong, G.Y., 2008. Bulk and single-particle mineralogy of Asian dust and a comparison with its source soils. J. Geophys. Res. [Atmos.] 113, D02208.
Journet, E., Balkanski, Y., Harrison, S.P., 2014. A new data set of soil mineralogy for dust-cycle modeling. Atmos. Chem. Phys. 14 (8), 3801–3816.
Junta de Andalucía, 2021a. Monthly air quality reports (1997-present). Retrieved from: https://www.juntadeandalucia.es/medioambiente/portal/landing-page-%C3%ADndice/-/asset_publisher/zX2ouZa4r1Rf/content/informes-mensuales-de-calidad-del-aire/20151?categoryVal=.
Junta de Andalucía, 2021b. Red de Vigilancia de la Calidad del Aire de Andalucía. Retrieved from: https://www.juntadeandalucia.es/temas/medio-ambiente/emisiones/calidad.html.
Kalashnikova, O.V., Sokolik, I.N., 2004. Modeling the radiative properties of nonspherical soil-derived mineral aerosols. J Quant Spectrosc Ra 87 (2), 137–166.
Kandler, K., Benker, N., Bundke, U., Cuevas, E., Ebert, M., Knippertz, P., Rodríguez, S., Schütz, L., Weinbruch, S., 2007. Chemical composition and complex refractive index of Saharan Mineral Dust at Izaña, Tenerife (Spain) derived by electron microscopy. Atmos. Environ. 41 (37), 8058–8074.
Kemnitz, H., Lucke, B., 2019. Quartz grain surfaces–A potential microarchive for sedimentation processes and parent material identification in soils of Jordan. Catena 176, 209–226.
Korotev, R.L., 2009. "Rare Earth Plots" and the Concentrations of Rare Earth Elements (REE) in Chondritic Meteorites. Retrieved from. http://meteorites.wustl.edu/goodstuff/ree-chon.htm.
Senthil Kumar, R., Rajkumar, P., 2014. Characterization of minerals in air dust particles in the state of Tamilnadu, India through FTIR, XRD and SEM analyses. Infrared Phys. Technol. 67, 30–41.
Kumara, G.H.A.J.J., Hayano, K., Ogiwara, K., 2012. Image analysis techniques on evaluation of particle size distribution of gravel. Int. J. Geomate 3 (1), 290–297.
Laveuf, C., Cornu, S., 2009. A review on the potentiality of Rare Earth Elements to trace pedogenetic processes. Geoderma 154 (1-2), 1–12.
Lequy, É., Legout, A., Conil, S., Turpault, M.-P., 2013. Aeolian dust deposition rates in Northern French forests and inputs to their biogeochemical cycles. Atmos. Environ. 80, 281–289.
Lequy, E., Avila, A., Boudiaf Nait Kaci, M., Turpault, M.-P., 2018. Atmospheric deposition of particulate matter between Algeria and France: Contribution of long and short-term sources. Atmos. Environ. 191, 181–193.
López-Quirós, A., Barbier, M., Martín, J.M., Puga-Bernabéu, Á., Guichet, X., 2016. Diagenetic evolution of Tortonian temperate carbonates close to evaporites in the Granada Basin (SE Spain). Sed. Geol. 335, 180–196.
Lyamani, H., Olmo, F.J., Alados-Arboledas, L., 2005. Saharan dust outbreak over southeastern Spain as detected by sun photometer. Atmos. Environ. 39 (38), 7276–7284.
Mahaney, W.C., 2002. Atlas of sand grain surface textures and applications. Oxford University Press, New York.
Marques, R., Prudêncio, M.I., Dias, M.I., Rocha, F., 2011. Patterns of rare earth and other trace elements in different size fractions of clays of Campanian-Maastrichtian deposits from the Portuguese western margin (Aveiro and Taveiro Formations). Chem. Erde 71 (4), 337–347.
Márquez, R., 2012. El cuarzo de la fracción arena fina en suelos de la provincia de Granada (Doctoral dissertation). Universidad de Granada, Granada.
Marticorena, B., 2014. Dust Production Mechanisms. In: Knippertz, P., Stuut, J.B. (Eds.), Mineral Dust. Springer, Dordrecht, pp. 93–120.
Martín-García, J.M., Aranda, V., Gámiz, E., Bech, J., Delgado, R., 2004. Are Mediterranean mountains Entisols weakly developed? The case of Orthents from Sierra Nevada (Southern Spain). Geoderma 118, 115–131.
Martin-Garcia, J.M., Delgado, G., Sanchez-Maranon, M., Parraga, J.F., Delgado, R., 1997. Nature of dioctahedral micas in Spanish red soils. Clays Clay Miner. 32 (1), 107–121.
Martín-García, J.M., Márquez, R., Delgado, G., Sánchez-Marañón, M., Delgado, R., 2015. Relationships between quartz weathering and soil type (Entisol, Inceptisol and Alfisol) in Sierra Nevada (southeast Spain). Eur. J. Soil Sci. 66 (1), 179–193.
Martin-Ramos, J.D., 2004. Using XPowder: A software package for Powder X-Ray diffraction analysis. Granada, Spain.
McDonough, W.F., Sun, S.-s., 1995. The composition of the Earth. Chem. Geol. 120 (3-4), 223–253.
Menéndez, I., Derbyshire, E., Engelbrecht, J., von Suchodoletz, H., Zoeller, L., Dorta, P., Carrillo, T., Rodríguez De Castro, F.C.B., 2009. Saharan dust and the aerosols on the Canary Islands: past and present. In: Cheng, M., Liu, W. (Eds.), Airbone Particulates. Nova Science Publishers, New York, pp. 39–80.
Menéndez, I., Díaz-Hernández, J.L., Mangas, J., Alonso, I., Sánchez-Soto, P.J., 2007. Airborne dust accumulation and soil development in the North-East sector of Gran Canaria (Canary Islands, Spain). J. Arid Environ. 71 (1), 57–81.
Menéndez, I., Pérez-Chacón, E., Mangas, J., Tauler, E., Engelbrecht, J.P., Derbyshire, E., Cana, L., Alonso, I., 2014. Dust deposits on La Graciosa Island (Canary Islands, Spain): texture, mineralogy and a case study of recent dust plume transport. Catena 117, 133–144.
Menut, L., Pérez, C., Haustein, K., Bessagnet, B., Prigent, C., Alfaro, S., 2013. Impact of surface roughness and soil texture on mineral dust emission fluxes modeling. J. Geophys. Res. [Atmos.] 118 (12), 6505–6520.
Ministry for Ecological Transition and Demographic Challenge, 2019. Evaluación de la calidad del aire en España 2018, p. 208 (in Spanish). Retrieved from: https://www.miteco.gob.es/es/calidad-y-evaluacion-ambiental/temas/atmosfera-y-calidad-del-aire/informeevaluacioncalidadaireespana2018_tcm30-498764.pdf.
Ministry for Ecological Transition and Demographic Challenge, 2021. Histórico de informes de episodios naturales (in Spanish). Retrieved from: https://www.miteco.gob.es/es/calidad-y-evaluacion-ambiental/temas/atmosfera-y-calidad-del-aire/calidad-del-aire/evaluacion-datos/fuentes-naturales/anuales.aspx.
Morales-Baquero, R., Pulido-Villena, E., Reche, I., 2013. Chemical signature of Saharan dust on dry and wet atmospheric deposition in the south-western Mediterranean region. Tellus B Chem Phys Meteorol. 65 (1), 18720. https://doi.org/10.3402/tellusb:v65i0.18720.
Mourier, B., Poulenard, J., Chavel, C., Faivre, P., Carcaullet, C., 2008. Distinguishing subalpine soil types using extractable Al and Fe extractions and REE geochemistry. Geoderma 145, 107–120.
Muhs, D.R., Budahn, J., Skipp, G., Prospero, J.M., Patterson, D., Bettis III, E.A., 2010. Geochemical and mineralogical evidence for Sahara and Sahel dust additions to Quaternary soils on Lanzarote, eastern Canary Islands. Spain. Terra Nova 22 (6), 399–410.
Muhs, D.R., Prospero, J.M., Baddock, M.C., Gill, T.E., 2014. Identifying Sources of Aeolian Mineral Dust: Present and Past. In: Knippertz, P., Stuut, J.B. (Eds.), Mineral Dust. Springer, Dordrecht, pp. 51–74.
Nickling, W., 1983. Grain-size characteristics of sediment transported during dust storms. J. Sediment. Petrol. 53 (3), 1011–1024.
Nickovic, S., Vukovic, A., Vujadinovic, M., Djurdjevic, V., Pejanovic, G., 2012. High-resolution mineralogical database of dust-productive soils for atmospheric dust modeling. Atmos. Chem. Phys. 12 (2), 845–855.
Párraga, J., Martín-García, J.M., Delgado, G., Molinero-García, A., Cervera-Mata, A., Guerra, I., Fernández-González, M.V., Martín-Rodríguez, F.J., Lyamani, H., Casquero-Vera, J.A., Valenzuela, A., Olmo, F.J., Delgado, R., 2021. Intrusions of dust and iberulites in Granada basin (Southern Iberian Peninsula). Genesis and formation of atmospheric iberulites. Atmos. Res. 248, 105260. https://doi.org/10.1016/j.atmosres.2020.105260.
Parviainen, A., Papaslioti, E.M., Casares-Porcel, M., Garrido, C.J., 2020. Antimony as a tracer of non-exhaust traffic emissions in air pollution in Granada (S Spain) using lichen bioindicators. Environ. Pollut. 263, 114482.
Prospero, J., Ginoux, P., Torres, O., Nicholson, S.E., 2002. Environmental characterization of global sources of atmospheric soil dust identified with the NIMBUS 7 total ozone mapping spectrometer (TOMS) absorbing aerosol product. Rev. Geophys. 40 (1), 1002.
Prudêncio, M.I., Braga, M.A.S., Gouveia, M.A., 1993. REE mobilization, fractionation and precipitation during weathering of basalts. Chem. Geol. 107, 251–254.
Querol, X., Alastuey, A., Rodriguez, S., Plana, F., Ruiz, C. R., Cots, N., Massagué, G., Puig, O., 2001. PM10 and PM2.5 source apportionment in the Barcelona Metropolitan area, Catalonia, Spain. Atmos. Environ. 35 (36), 6407–6419.

Reche, I., D'Orta, G., Mladenov, N., Winget, D.M., Suttle, C.A., 2018. Deposition rates of viruses and bacteria above the atmospheric boundary layer. ISME J. 12 (4), 1154–1162.
Reid, E.A., Reid, J.S., Meier, M.M., Dunlap, M.R., Cliff, S.S., Broumas, A., Perry, K., Maring, H., 2003. Characterization of African dust transported to Puerto Rico by individual particle and size segregated bulk analysis. J. Geophys. Res. [Atmos.] 108 (D19), 8591.
Rodríguez, S., Alastuey, A., Alonso-Pérez, S., Querol, X., Cuevas, E., Abreu-Afonso, J., Viana, M., Pérez, N., Pandolfi, M., De la Rosa, J., 2011. Transport of desert dust mixed with North African industrial pollutants in the subtropical Saharan Air Layer. Atmos. Chem. Phys. 11 (13), 6663–6685.
Rodríguez, S., Cuevas, E., Prospero, J.M., Alastuey, A., Querol, X., López-Solano, J., García, M.I., Alonso-Pérez, S., 2015. Modulation of Saharan dust export by the North African dipole. Atmos. Chem. Phys. 15, 7471–7486.
Rodriguez-Navarro, C., Di Lorenzo, F., Elert, K., 2018. Mineralogy and physicochemical features of Saharan dust wet deposited in the Iberian Peninsula during an extreme red rain event. Atmos. Chem. Phys. 18 (13), 10089–10122.
Rodríguez-Ruiz, M., Abad, I., Bentabol, M.J., 2019. Permo-triassic clastic rocks from the Ghomaride complex and Federico units (Rif Cordillera, N Morocco): An example of diagenetic-metamorphic transition. Minerals 9 (12), 738.
Russo, A., Sousa, P.M., Durão, R.M., Ramos, A.M., Salvador, P., Linares, C., Díaz, J., Trigo, R.M., 2020. Saharan dust intrusions in the Iberian Peninsula: Predominant synoptic conditions. Sci. Total Environ. 717, 137041.
Schepanski, K., 2018. Transport of mineral dust and its impact on climate. Geosciences 8 (5), 151.
Scheuvens, D., Kandler, K., 2014. On Composition, Morphology, and Size Distribution of Airborne Mineral Dust. In: Knippertz, P., Stuut, J.B. (Eds.), Mineral Dust. Springer, Dordrecht, pp. 15–49.
Scheuvens, D., Schütz, L., Kandler, K., Ebert, M., Weinbruch, S., 2013. Bulk composition of northern African dust and its source sediments—A compilation. Earth-Sci. Rev. 116, 170–194.
Schultz, L.G., 1964. Quantitative interpretation of mineralogical composition from X-ray and chemical data for the Pierre Shale. U.S. Geol. Surv. Prof. Pap. 391 C.
Strunz, H., Tennyson, C., 1982. Mineralogical Tables. Akademie-Verlaggesellschaft. Geest & Portig, Leipzig.
Sweet, D.E., Brannan, D.K., 2016. Proportion of glacially to fluvially induced quartz grain microtextures along the Chitina river, SE Alaska. USA. J. Sediment. Res. 86 (7), 749–761.
Torfstein, A., Teutsch, N., Tirosh, O., Shaked, Y., Rivlin, T., Zipori, A., Stein, M., Lazar, B., Erel, Y., 2017. Chemical characterization of atmospheric dust from a weekly time series in the north Red Sea between 2006 and 2010. Geochim. Cosmochim. Acta 211, 373–393.
Valenzuela, A., Olmo, F.J., Lyamani, H., Antón, M., Quirantes, A., Alados-Arboledas, L., 2012. Analysis of the columnar radiative properties retrieved during African desert dust events over Granada (2005–2010) using principal plane sky radiances and spheroids retrieval procedure. Atmos. Res. 104–105, 292–301.
Vera, J.A. (Ed.), 2004. Geología de España. SGE-IGME, Madrid.
Vos, K., Vandenberghe, N., Elsen, J., 2014. Surface textural analysis of quartz grains by scanning electron microscopy (SEM): From sample preparation to environmental interpretation. Earth-Sci. Rev. 128, 93–104.
Wang, R.D., Li, Q., Zhang, C.L., Wang, Z.T., Guo, Z.L., Chang, C.P., Li, J.F., 2021. Comparison of dust emission ability of sand desert, gravel desert (Gobi), and farmland in northern China. Catena 201, 105215.
Wang, X., Wen, H., Shi, J., Bi, J., Huang, Z., Zhang, B., Zhou, T., Fu, K., Chen, Q., Xin, J., 2018. Optical and microphysical properties of natural mineral dust and anthropogenic soil dust near dust source regions over northwestern China. Atmos. Chem. Phys. 18 (3), 2119.
WHO, 2013a. IARC: Outdoor air pollution a leading environmental cause of cancer deaths. Press release n° 221. Retrieved from: https://www.iarc.who.int/wp-content/uploads/2018/07/pr221_E.pdf.
WHO, 2013b. Health effects of particulate matter. Policy implications for countries in eastern Europe, Caucasus and central Asia. Retrieved from: https://www.euro.who.int/_data/assets/pdf_file/0006/189051/Health-effects-of-particulate-matter-final-Eng.pdf.
WHO, 2018. Ambient (outdoor) air pollution. Retrieved from: https://www.who.int/news-room/fact-sheets/detail/ambient-(outdoor)-air-quality-and-health.
Xie, Y., Meng, J., Guo, L., 2014. REE geochemistry of modern eolian dust deposits in Harbin city, Heilongjiang province, China: Implications for provenance. Catena 123, 70–78.
Xie, Y., Yuan, F., Zhan, T., Kang, C., Chi, Y., 2018. Geochemical and isotopic characteristics of sediments for the Hulun Buir Sandy Land, northeast China: implication for weathering, recycling and dust provenance. Catena 160, 170–184.